Infrared joining strength and interfacial microstructures of Ti–48Al–2Nb–2Cr intermetallics using Ti–15Cu–15Ni foil

S.J. Lee, S.K. Wu*

Institute of Materials Science and Engineering, National Taiwan University, Taipei, Taiwan 106

Abstract

Infrared joining of Ti–48Al–2Nb–2Cr using Ti–15Cu–15Ni (wt%) foil as brazing filler metal was investigated at the temperature range of 1100∼1200°C for 30∼60 s in a flowing argon environment. The compressive tests show three types of fracture morphologies in which type I fails at the joint interface, but types II and III are fractured in the base-metal with the crack direction parallel to and perpendicular to the loading axis, respectively. Most of joined specimens were fractured through the base metal indicating that the infrared joined interface has relatively good joint strength. The compressive strength of type I specimen is about 319–322 MPa. Experimental results show that the shorter the real holding time or the higher the joining temperature, the larger the strength variation will be. The observed interfacial microstructures of Ti–48Al–2Nb–2Cr joint interfaces indicate that seven characteristic zones can be distinguished in the joint interfaces and each characteristic structure corresponds to one or more stable phases at T_w temperature. The observed microstructures and their evolutions of each zone are explained in detail in this study. The major difference between joint interfaces of Ti–48Al–2Nb–2Cr and Ti$_{50}$Al$_{50}$ alloys takes place on the base-metal interface zone and the columnar two-phase zone. The existence of Nb and Cr atoms in Ti–48Al–2Nb–2Cr alloy also has some influences on the microstructural evolution of the columnar two-phase zone and the continuous α_2-layer. © 1998 Elsevier Science Ltd. All rights reserved.

Keywords: A. Titanium aluminides, based on TiAl; B. Mechanical properties at ambient temperature; C. Infrared joining; D. Microstructure, phase interface

1. Introduction

With highly attractive properties of low density and high-temperature strength retention, titanium–aluminide alloys based on gamma TiAl have an excellent potential to become one of the most important high-temperature structural materials [1–4]. Recently, the properties of gamma alloys have been remarkably improved through alloy design and microstructure control to meet requirements for some gas-turbine and automobile engine components that may be used up to 760°C [4]. However, appropriate joining techniques are indispensable for the full utilization of these materials due to the persistent barriers of their low fracture toughness and poor fabricability at low to intermediate temperatures [1–4].

In order to develop a suitable joining process, several joining techniques, including welding [5–7], diffusion-bonding [8–10] and infrared joining [11–14], have been studied to improve the weldability of titanium alumi-

nides. In welding, welding cracks cannot easily be avoided [5] and optimum weld structures and properties can be obtained by properly controlling the weld cooling rates [6,7]. As to diffusion-bonding, Nakao et al. [8] investigated the diffusion bonding of Ti–52Al and the acquired joint tensile strength at room temperature was about 225 MPa. Yan and Wallach [9] studied the solid-state diffusion bonding and transient-liquid-phase bonding of Ti–48Al. Bonds made by solid-state diffusion (1200°C×20 MPa) show comparatively good shear strength of about 225–260 MPa, as compared with the strength of parent material which is about 275–310 MPa. Very recently, Cam et al. [10] investigated the solid-state diffusion bonding of γ-TiAl (47Al + Cr–Mn–Nb–Si–B) under different bonding temperatures of 925–1100°C and different bonding pressures of 20–40 MPa. The wide joint strengths ranging from 200–450 MPa have been obtained by the room temperature micro-tensile tests. Although solid-bonds with rather good joint properties can be obtained by diffusion bonding, the long processing time and the high corresponding

---

* Corresponding author.

operation/installation costs may render this joining method useless for practical applications, especially for joining large-sized workpieces. Infrared joining, one of the RIPs (rapid isothermal process), can offer a very quick and cost-effective method for joining advanced materials [11]. This process was adopted to join titanium-aluminide mainly due to its sensitive thermal response which plays great influences on the joint interfacial microstructures.

The infrared joining of equiatomic TiAl alloy has been studied by Lin et al. [11,12] and Lee et al. [13,14]. The detailed microstructure morphologies [13] and its evolutional mechanism [14] of TiAl joint interfaces using Ti–15Cu–15Ni foil as brazing filler metal have been effectively revealed by the sensitive thermal responses of infrared process. However, the joint strength of TiAl alloys infrared joined using Ti–15Cu–15Ni foil as brazing filler metal has still not been reported. The aim of this study is to investigate the joint strength and the interfacial microstructures of the infrared joining of Ti–48Al–2Nb–2Cr intermetallics. This alloy was selected as the joining base-metal mainly due to its highly potential use in industry. Based on results of previous studies [13,14], the complex interfacial microstructures and their effects on the joint strength of Ti–48Al–2Nb–2Cr alloys can be clearly explained.

2. Experimental procedures

A series of infrared joining with different joining conditions were conducted using Ti–48Al–2Nb–2Cr (at%) alloy as the joined base-metal. Joining temperature (T_w) of 1100–1200°C and holding time (t_w) of 30–60 s were used. A conventional tungsten vacuum arc remelting (VAR) technique was employed to prepare this base-metal. The as-melted Ti–48Al–2Nb–2Cr button was homogenized at 1200°C×50 h in a $7×10^{-5}$ torr vacuum furnace and then followed by furnace cooling. The homogenized button was cut into 10×8×3 mm and 5×8×3 mm specimens by wire-cutting. These specimens were polished to a 1200 grit finish and then cleaned ultrasonically in acetone prior to infrared joining.

A Ti–15Cu–15Ni (wt%) foil with 50 μm thickness (WESGO commercial product, with commercial name Ticuni foil) was used as the brazing filler metal. Ticuni is a clad-laminated brazing filler metal (LBFM) foil [15], whose solidus and liquidus temperatures are 910 and 960°C, respectively. The specimens, with Ticuni foil, were then carefully assembled into a special designed graphite clamp to form a single overlap compressive shear assembly, as shown in Fig. 1. A slight pressure was applied to keep all the parts in place by graphite screws. Prior to the heating cycle, the infrared chamber was pre-vacuumized and then argon was purged for
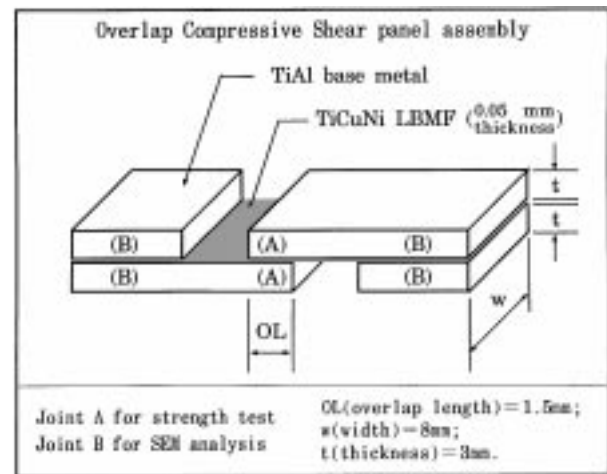

Fig. 1. The geometry of the single overlap compressive shear specimens. Joint area (A) for joint strength test and joint areas (B) for microstructural analyses.

approximately 60 s. During the heating, argon continuously flowed through the heating chamber to minimize the oxidation of specimens. The processing temperature was monitored with a R type Pt/Ir thermocouple fixed on the specimen's upper surface by graphite clamps. After joining in the infrared furnace, joint area A of specimen shown in Fig. 1 can be used to estimate the bonding strength, and joint areas B are for interfacial microstructure analyses.

The equipment for infrared joining used in this study was ULVAC SINKO-RIKO RHL-P610C type infrared gold image furnace. Its maximum operating temperature was 1300°C. Five infrared joining conditions, (1) #1: 1150°C×30 s, (2) #2: 1150°C×42 s, (3) #3: 1150°C×60s, (4) #4: 1100°C×42 s and (5) #5: 1200°C×42 s, were set and controlled by the EUROTHERM 818 type temperature controller. Two specimens were joined for each joining condition. The heating rate of 3000°C min^{-1}. was adopted for all conditions. Fig. 2 is the real temperature versus real time profile for the sample #3 during the whole joining process. In Fig. 2, there are four main stages: (I) heating, (II) dissolution, (III) isothermal solidification and (IV) cooling stages [16]. T_w, T_s, t_w and t_w' of Fig. 2 are defined as the joining temperature, the solidus of Ticuni filler-metal, the programmer setting holding-time and the real holding time, respectively. Typically, 30, 27 and 37 s is required for the specimen's temperature to be raised to the set T_w temperature of 1150, 1100 and 1200°C, respectively. Therefore, the real holding time (t_w') for samples #1~#5 was 0, 12, 30, 15 and 5 s, respectively. Upon terminating the power, the specimen temperature dropped instantly since the furnace wall was not heated up by the infrared processing. Normally, the specimen cooled to below 500°C in about 120 s and the cooling rate between T_w and T_s is about 600°C min^{-1}. After the compressive strength tests, joint
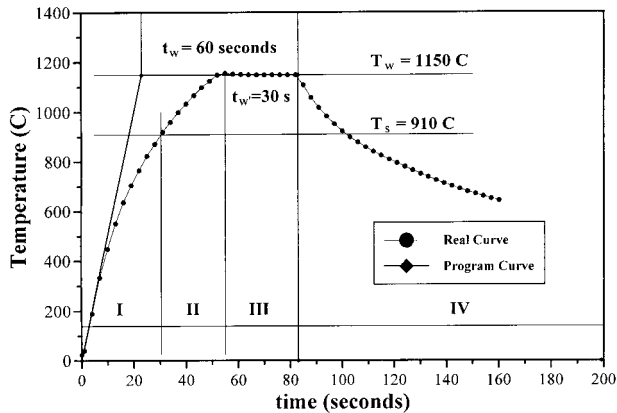
Fig. 2. The real temperature versus real time chart of sample #3. The entire joining process can be divided into four main stages: (I) heating, (II) dissolution, (III) isothermal solidification and (IV) cooling stages. T_w, T_s, t_w and t'_w are the joining temperature, the solidus of Ticuni filler-metal, the programmer setting holding time and the real holding time, respectively.

areas B of specimens were cut, mounted and polished, and then etched with the Kroll's reagent (2 ml HF, 4 ml HNO_3 and 100 ml H_2O) for SEM and EPMA examinations. At the same time, fracture surfaces of joint areas A of specimens were observed by SEM and EPMA and analyzed by X-ray diffraction (XRD).

Microstructures were observed by Nikon 104 OM and Philips 515 SEM. The JEOL JXA-8600SX EPMA was utilized to take the images, line-scanning profile (LSP) and quantitative composition of joined interface. The EPMA was operated at 15 KV with a probe current 100 nA. XRD analysis with Cu K_α X-ray was conducted by using a Philips 1710 X-ray diffraction equipment carried out at 30 KV and 20 mA. The compressive strength test was conducted at room temperature by Sintech 20/D instrument with a strain rate 0.25 mm min^{-1}.

3. Experimental results

3.1. The compressive strength tests

Prior to the compressive test, all outside planes of infrared joined specimens shown in Fig. 1 were ground to make sure that they are parallel and perpendicular to each other and to get rid of the overflowed residual filler metal on these outside planes. However, the over-flowed residual filler metal still exists on the corners of inside planes of infrared joined specimens, as arrows shown in Fig. 3(b). Fig. 3(a) shows the loading of this test at two end planes of specimen. The measured compressive strengths as a function of t_w and T_w are illustrated in Fig. 3(c) and (d), respectively. After testing, three different fractured morphologies I, II and III (marked by ■, ● and ◆, respectively) can be observed in all tested

specimens, as shown in Fig. 3(a). Type I fails just through the joint interface, but cracks of types II and III are near-parallel (II) or vertical (III) to the loading direction and occur away from the joint interface. The detailed fracture morphologies will be further discussed in Section 3.3 through the microstructural examination. Most of samples (eight of 10) were fractured through the base metal, i.e. types II and III fracture. This feature indicates that joint interfaces have relatively good joint strength. The other two specimens (type I fracture) show the real joint strength (about 319–322 MPa) of infrared joint interfaces. As compared with the reported shear strength (about 225–260 MPa) of diffusion-bonding ones [8], the infrared joint interface exhibits rather good joint strength.

From Fig. 3(c), at constant $T_w = 1150°C$, the acquired joint strength increases with increasing t_w. The joining condition of $t_w = 30$ s. ($t'_w = 0$ s) has the lowest joint strength and the largest strength variation, while the one of $t_w = 60$ s ($t'_w = 30$ s) behaves just in reverse. From Fig. 3(d), when a constant $t_w = 42$ s is used, the measured upper strengths of specimens joined at $T_w = 1100$, 1150 and 1200°C are very close to each other. However, the specimen with higher T_w has larger strength variation, as shown in Fig. 3(d).

The strength variation appeared in Fig. 3(c) and (d) can be explained by the real holding time (t'_w) of each specimen. The results of Fig. 3(c) and (d) show that the shorter the t'_w, the larger the strength variation will be. Because the microstructure of TiAl intermetallics is highly sensitive to its composition and heat-history [17]. The shorter t'_w may cause a larger temperature gradient between the outer and inner parts of specimen and then produce more microstructural difference in the same specimen during the cooling. For example: the t'_w of samples #1 and #5 is 0 and 5 s, respectively, therefore they exhibit a rather large strength variation, as shown in Fig. 3(c) and (d).

3.2. The microstructures of joint interfaces

After compressive testing, the cross-sectioned microstructures of areas B of infrared joining specimens were examined under SEM and EPMA. Fig. 4(a)–(e) shows the secondary electron images (SEIs) of joint interfaces for five different joining conditions. All joint interfaces show distinct multilayered structures and demonstrate that both T_w and t_w greatly affect the microstructural evolution. From Fig. 4, the major difference between each photography is the morphologies of black columnar strips which have been proven to be the α_2-Ti_3Al phase at T_{room} by EPMA WDS analyses and has relatively low Cu and Ni contents. In general, the brighter interfacial areas in Fig. 4 are Cu- and Ni-rich regions and the darker ones are Al-rich regions. According to our previous studies on the interfaces of infrared joining
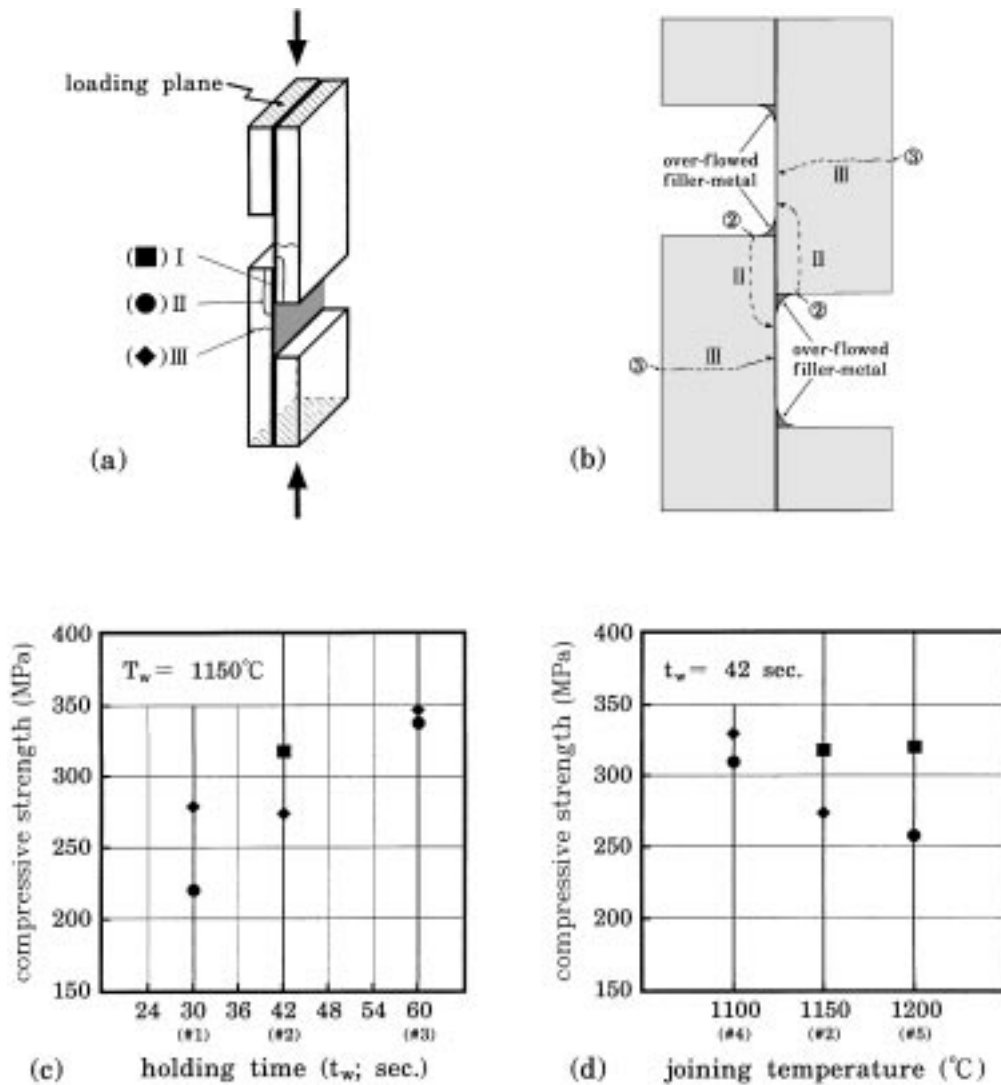
Fig. 3. (a) The stereograph showing the compressive configuration and three types of fracture morphologies; (b) the front-viewed profile schematically indicating the crack initiated sites and the propagated paths of types II and III fracture morphologies; (c) and (d) showing the acquired compressive strength at constant $T_w = 1150°C$ and $t_w = 42$ s, respectively.

γ-Ti$_{50}$Al$_{50}$ specimens, seven characteristic zones can be distinguished [13,14]. These seven zones are found also to exist in the Ti–48Al–2Nb–2Cr joint interfaces. In Fig. 4, I~VII express these seven characteristic zones which are the base-metal zone (I), the base-metal interface zone (II), the columnar two-phase zone (III), the discontinuous precipitation zone (IV), the α_2 layer (V), the netted precipitation zone (VI) and the residual filler-metal zone (VII). They will be further discussed in Section 4.2, with more detailed microstructures and the corresponding binary Ti–Al phase diagram.

3.3. The fracture surface examinations

Fig. 5 shows the side-view and top-view of fracture surfaces of two type I specimens which failed at the joint interface. The fracture of specimen joined at 1200°C×

42 s [Fig. 5(a)] is observed to take place mainly along the base-metal interface zone (Zone II) with joint strength about 322 MPa. Its fracture surface [Fig. 5(b)] is rather flat which indicates the characteristic of brittle fracture at zone II. Specimen joined at 1150°C×42 s [Fig. 5(c)] fractured mainly along the residual filler metal zone (Zone VII) with joint strength 319 MPa. Its fracture surface [Fig. 5(d)] shows a relatively rough topography which indicates some ductile fracture nature at the residual filler metal zone. The XRD analysis of Fig. 5(d) shows that the Ti$_3$Al, Ti$_2$Cu and Ti(Cu,Ni) are the major phases near the fracture surface (Lee and Wu, 1997, unpubl. results). An EPMA test indicates that the spheres shown by arrows exists in Fig. 5(d) are Ti$_3$Al(α_2) phase.

Fig. 6(a) shows a typical fracture photography of type II specimen which is joined at 1150°C×60 s with a measured compressive strength of 338 MPa. From Fig. 6(a),
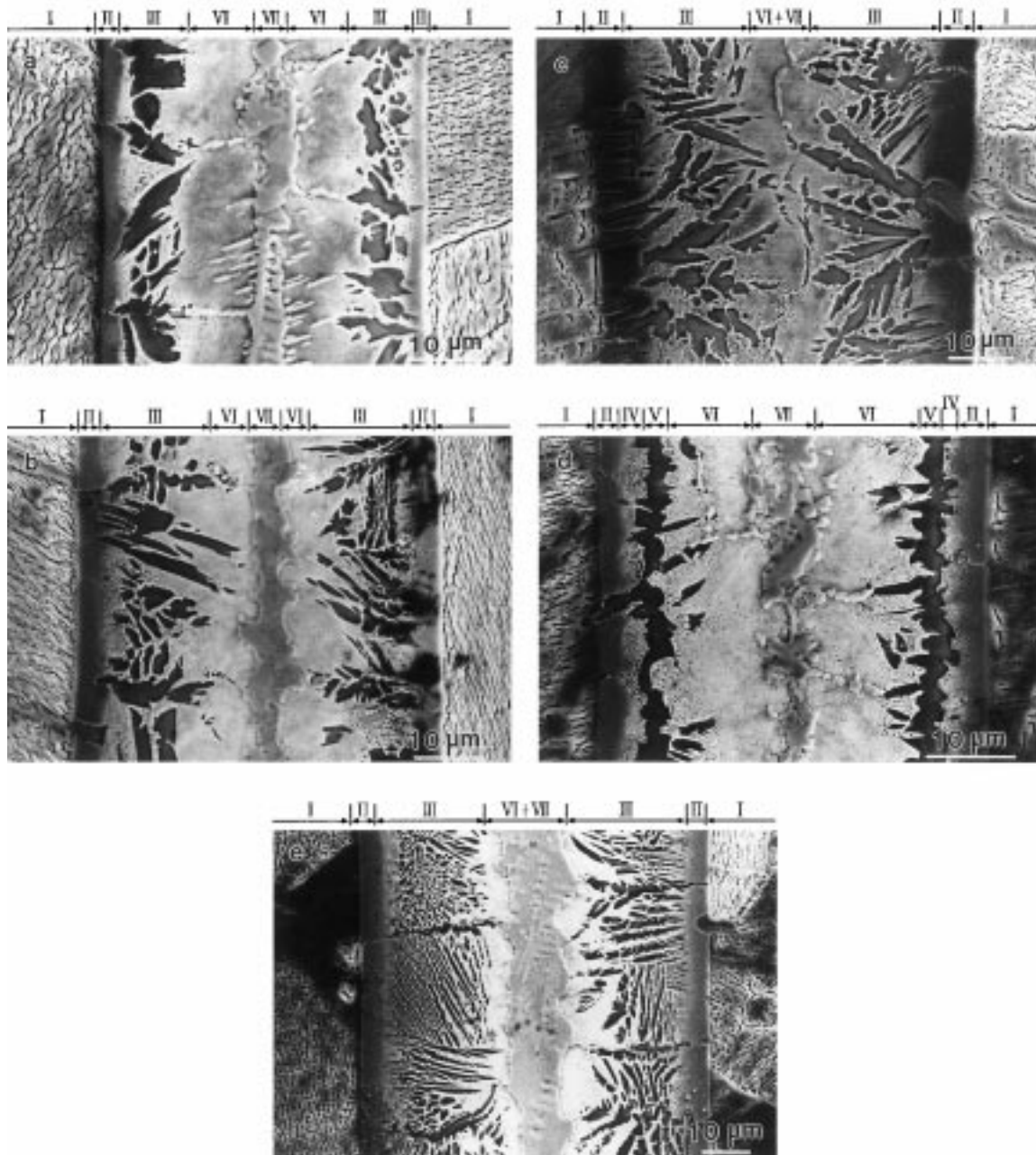
Fig. 4. The cross-sectioned interfacial microstructures of five different joining conditions of Ti–48Al–2Nb–2Cr base metal for: (a) #1: 1150°C×30 s; (b) #2: 1150°C×42 s; (c) #3: 1150°C×60 s; (d) #4: 1100°C×42 s; and (e) #5: 1200°C×42 s. I~VII express the seven characteristic interfacial zones discussed in the text.

it is clear that cracks were initiated at the margins of overflowed residual filler metal (as indicated by arrows) and then propagated parallel to the joint interface, i.e. parallel to the loading axis of tested specimen. Certainly, the margins of these residual filler-metal which exists at the corners of inside-planes might become the stress concentration sites and enlarge the stress during the compressive test. This causes failures easily to take place in the base-metal, instead of at the interface, as shown in Fig. 3(b). Due to the brittle nature of the base-

metal, if cracks initiated at the pair sites of 2 shown in Fig. 3(b), they would propagate in the direction parallel with the joint interface under further compressive loading, and then the type II fracture occurs. At the same time, the bending moment can be induced in the specimen configuration of Fig. 1 during the compressive test, cracks also have the possibility to be initiated at the places of maximum bending moment in the base-metal, as the pair sites of 3 shown in Fig. 3(b). Once cracks were formed in such a way, they will propagate and
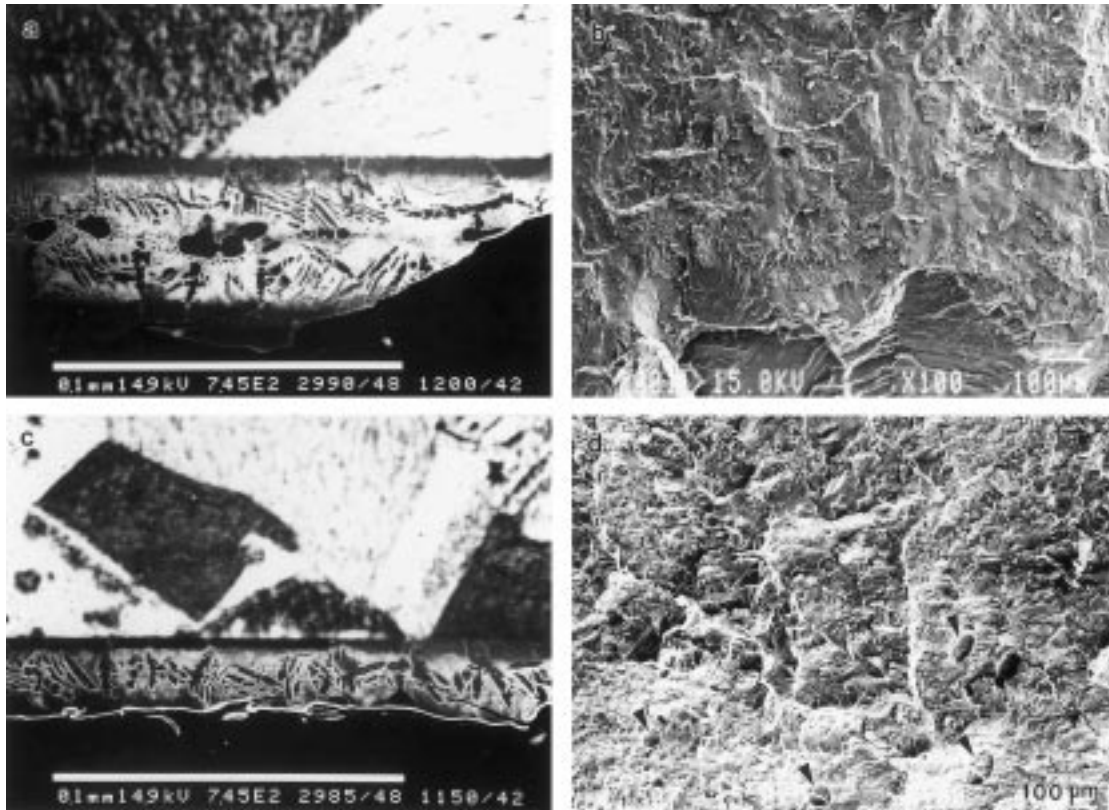
Fig. 5. The side-view and top-view of fracture surfaces of the two type I specimens which is failed just at the joint interface: (a) and (b) joined at 1200°C×42 s with joint strength JS = 322 MPa; (c) and (d) joined at 1150°C×42 s with JS = 319 MPa.

cross over the base-metal with a perpendicular direction, as shown in Fig. 6(b). Four out of ten specimens had fractured by type III in this study.

4. Discussion

4.1. The microstructural evolution of joint interfaces

Referred to previous studies [13,14], the multilayered interfacial microstructures shown in Fig. 4 are mainly formed by the atomic interdiffusion at high joining temperature T_w (stage III of Fig. 2), which included the primary isothermal solidification of a new solid layer and the following solid-state interdiffusion between this layer and the base metal. Due to the solid-state interdiffusion, the multilayered interfacial structure forms first at T_w, and then it phase-transforms to the room-temperature microstructures during the rapid cooling (stage IV of Fig. 2). The successive diffusion of Al atoms from the base-metal into the joint was found to be the main controlling factor pertaining to the interfacial microstructures. Seven characteristic zones of room-temperature microstructures can be distinguished in the joint interfaces and each zone corresponds to one or more stable phases at T_w. These seven characteristic zones and their evolutional processes are discussed as follows.

4.2. The seven characteristic zones

Compared with previous studies [13,14], it can be found that the interfacial microstructures acquired in this study (Fig. 4) still have some differences with $Ti_{50}Al_{50}$ joint interfaces. In order to investigate the characteristics of Ti–48Al–2Nb–2Cr joint interfaces, several analyses were carried out under SEM and EPMA, including SEI (secondary electron image), BEI (back-scattering electron image), LSP (line scanning profile) and WDS (wave dispersed spectrometer) quantitative analyses.

4.2.1. Zone I: the base-metal zone

The base-metal zone (Zone I) indicates the microstructure of base-metal after infrared joining. The microstructure of as-homogenized Ti–48Al–2Nb–2Cr alloy is a nearly duplex lamellar structure consisting of alternative γ/α_2 lamellae and equiaxed γ grains [1,10], as shown in Fig. 7. Fig. 7(a) and (b) are the magnified SEI and BEI of interfacial microstructures corresponding to the right center region of Fig. 4(c). In Fig. 7, the white and long strips are α_2 phase at T_{room} and are the high Al% α-phase at T_w. The gray regions with many black cracks inside are γ-plates (γ_{pl}) or primary γ-grains (γ_g), whose cracks are created due to the stress-induced corrosion cracking by the etching of Kroll's reagent [13,19].
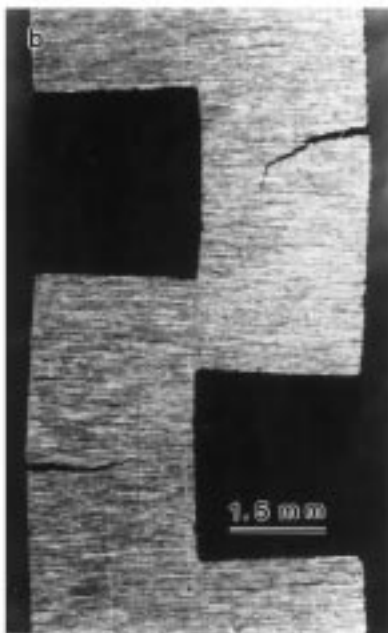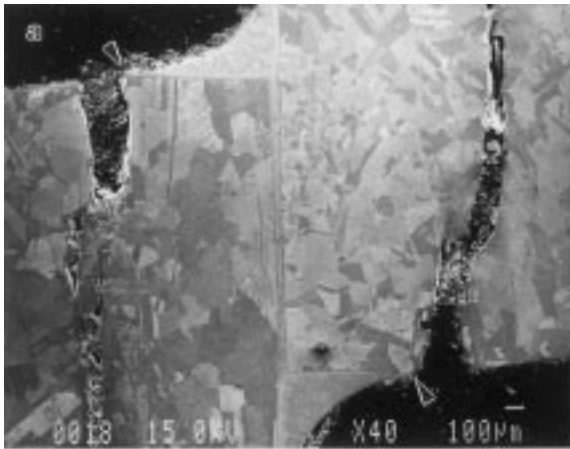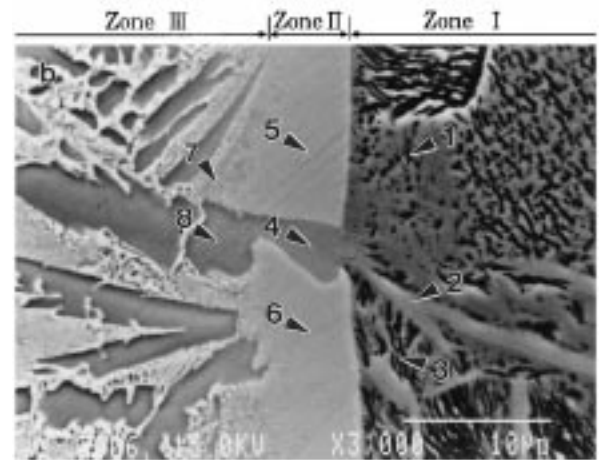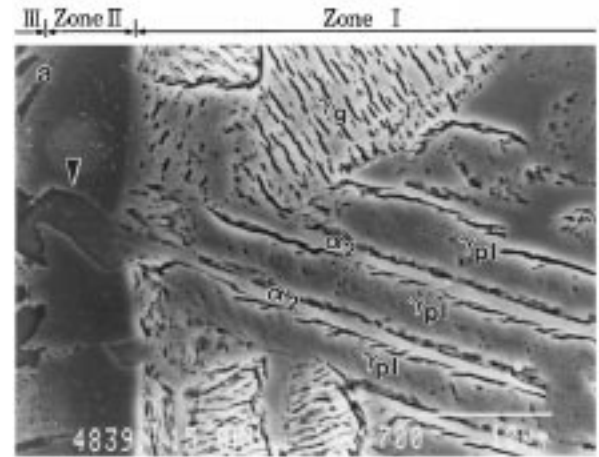
Fig. 6. The cross-section of samples with (a) type II fracture morphology which is joined at 1150×60 s with JS = 338 MPa and (b) type III fracture morphology which is joined at 1150×42 s with JS = 275 MPa.

Element Sites	Ti	Al	Cu	Ni	Nb	Cr	Remarks
1.	47.42	48.68	0.05	0.03	2.08	1.82	γ-phase in Zone I
2.	53.53	42.01	0.30	0.11	1.84	2.41	α-strip in Zone I
3.	50.43	45.20	0.06	0.03	1.97	2.31	(α + γ) in Zone I
4.	55.78	38.05	0.45	0.37	1.81	1.54	original α-phase in Zone II
5.	58.12	34.01	1.42	1.44	2.12	1.89	γ-transformed α in Zone II
6.	58.97	34.10	1.50	1.44	2.18	1.81	γ-transformed α in Zone II
7.	67.87	29.10	0.80	0.33	1.28	0.62	block α-column in Zone III
8.	62.78	27.06	3.86	3.42	1.58	1.46	white β-area in Zone III

Fig. 7. (a) The SEI microstructures of the base-metal zone (I) and the base-metal interface zone (II), of the joint interface corresponding to Fig. 4(c); (b) the BEI microstructure with detected sites (marked by 1∼8) and the accessory composition table of the EPMA WDS quantitative analyses detected on or near the base-metal interface zone (II) related to Fig. 7(a). The corresponding zones and phases of each detected site are also shown in the last columnar of the accessory table.

Fig. 7 and the accessory table indicate the detailed WDS analytic results detected on several interesting sites marked by 1∼8. The corresponding zones and phases of each detected site are also shown in the last column of the accessory table of Fig. 7. From Fig. 7(b), the γ-phase (site 1) and α-strip (site 2) in Zone I have 48.6% and 42.0% Al-content, respectively. With some α-phase inside, site 3 shows intermediate Al-content which is about 45%. These features are well consistent with the points B and A indicated on the T_w isotherm in Ti–Al phase diagram shown in Fig. 8. This α + γ two-phase consisted in the base-metal zone (Zone I) of Ti–48Al–2Nb–2Cr alloy will cause more complex interfacial reaction than $Ti_{50}Al_{50}$ (only single γ-phase) inter-

faces [13,14], especially on forming the base-metal interface zone (Zone II), as discussed in the following.

4.2.2. Zone II: the base-metal interface zone

Zone II evolved out of Zone I due to the successive diffusion of Al atoms from the base-metal to the filler-metal at T_w. Based on the multiphase diffusion theories in ternary solid-state interdiffusion system [20,21], the compositional diffusion-path of a diffusion-couple interface must continuously and smoothly vary in single-phase
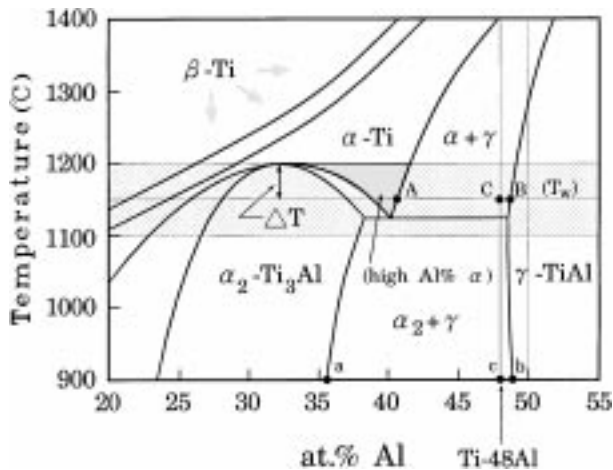
Fig. 8. The central portion of Ti–Al binary phase diagram [2,18].

regions, but it will abruptly jump or cross-over the two-phased domains. Because the composition of γ phase (point B in Fig. 8) at T_w is just on the boundary of γ-TiAl single-phase region, thus, once its Al% decreases due to the Al atom diffusion-out, the original γ-phase regions near the joint interface will directly change into the high Al% α-phase (point A in Fig. 8). At the same time, the original α-phase regions (as arrow indicated in Fig. 7(a)) will keep their phase due to its lower Al-content. This causes the formation of the base-metal interface zone (Zone II), as shown in Fig. 7. In other words, the base-metal interface zone (II) of Ti–48Al–2Nb–2Cr joint interface should be single α phase with two origins, one is original α-phase and the other is γ-transformed one at T_w. Due to different origins, both α areas in Zone II show distinguishable microstructural regions, as shown in Fig. 7.

The original α-phase in Zone II [site 4 in Fig. 7(b)] exhibits 38.0% Al-content and has rather low Cu- and Ni- contents, in which Al% is slightly lower than the α-strip in Zone I (site 2) due to some diffusion-out of Al atoms. The two γ-transformed α-phase sites in Zone II (sites 5 and 6) have similar Ti-, Nb-, and Cr- contents to the original α-phase (site 4), but they have higher Cu- and Ni-, and lower Al- contents than site 4. This phenomenon indicates that the inward diffusion of Cu and Ni atoms from the filler-metal also plays a role on the formation of Zone II and can be explained by the different activity of Cu and Ni atoms in α or β phase in Zone III. As mentioned in our previous study [14], the Cu and Ni atoms have higher activity coefficient in α-phase than in β-phase, thus they will be expelled from the already formed α-phase columns and diffuse out mainly along the β-phase areas existing between the α-columns. Because the original α-phase in Zone II (site 4) is an already formed α-column which is continuously extended to the Zone III, therefore, these inward diffused Cu and Ni atoms are more easily to diffuse into

the γ-transformed α-phase than into the original α one, and then result in the higher Cu- and Ni- contents in the γ-transformed α-phase. In addition, some atomic inter-diffusion also might occur at the interface of these two α-phase due to the above mentioned compositional difference existing between them. Thus, the original α-phase area in Zone II grows and seems to be a little bit wider than the original α-strip in Zone I, as also shown in Fig. 7(b).

During cooling from T_w to T_{room}, both α-phase regions in Zone II will transform into ordered α_2 phase with few small white precipitates shown in Fig. 7(a). The microstructural morphologies of Zones I and II discussed above are quite different from those in $Ti_{50}Al_{50}$ alloy. Zone II of $Ti_{50}Al_{50}$ alloy is just a single γ-phase with Al-content being less than 50 at% [13].

4.2.3. Zone III: the columnar α + β two-phase zone (CTZ)

Fig. 4(a)–(c) and (e), at $T_w = 1150$ or 1200°C, show that Zone (III) is the most characteristic zone in the interfaces. The 1150°C×42 s joint interface of Fig. 4(b) was selected as an example to express the typical CTZ microstructure, as shown in Fig. 9. In Fig. 9, the black columns are $Ti_3Al(\alpha_2)$-phase at T_{room} and are α-phase at T_w, the white areas are β-phase at T_w and are black α_2 matrix and white Cu(Ni)-rich precipitates at T_{room}. As mentioned in Sections 3.2. and 4.2.2., these black α-phase columns are Al-rich and the white β-phase areas are Cu- and Ni-rich. This elemental partition features that α-stabilized element (Al) is concentrated on α-phase and β-stabilized elements (Cu and Ni) are focused on β-phase [22]. This is the main reason to form the (α + β) two-phase columnar structure of Zone III. As shown in Fig. 7(b), the black α-phase in Zone III (site 7) indeed has higher Al- and much lower Cu- and Ni- contents than the white β-phase (site 8). Due to atomic inter-diffusion at T_w, it is reasonable to suggest that the longer the holding time t_w or the higher the joining temperature T_w, the wider the CTZ will be, as observed in Fig. 4.

During the CTZ formation in the interface, the original α-phase areas existing in Zone II can provide the necessary nucleation sites of the columnar α-phase strips in Zone III. Thus, the CTZ can be more easily formed in this study than in the $Ti_{50}Al_{50}$ joint interfaces. This is one of the reasons why the CTZ becomes the dominant zone in joint interfaces of Fig. 4. The continuity between the black columns in Zone III and the original α-phase in Zone II is frequently observed in this study, as shown in Figs. 4,7,9 and 10.

4.2.4. Zones IV and V: the discontinuous precipitation zone and α_2 layer

At $T_w = 1100$°C, the black α-phase columns integrate together to form a continuous layer (Zone V), as shown

in Fig. 4(d) and 10. Fig. 10 clearly shows that the continuous α_2 layer (Zone V) and the discontinuous precipitation zone (Zone IV) are the characteristic morphologies of the 1100°C×42 s joint interface. Zones IV and V are simultaneously formed in the joint interface when Zone III vanishes due to the longer t_w or the lower T_w. This feature is also observed in the Ti$_{50}$Al$_{50}$ infrared joined interface [13]. At T_w, Zones IV and V are high Al% α-phase and α_2-Ti$_3$Al phase, respectively [14].

This phenomenon also implies that the joining temperature T_w has great influence on the formation of α_2 phase. The lower the T_w, the greater the driving force for the α_2 phase to nucleate from the α-phase, thus, the continuous α_2 phase (Zone V) can more easily be formed in the joint interface at lower T_w, as shown in Fig. 4(d) of $T_w = 1100$°C. The EPMA WDS composition detection indicates that the α_2-Ti$_3$Al layer (Zone V) only dissolves very little Cu and Ni atoms.
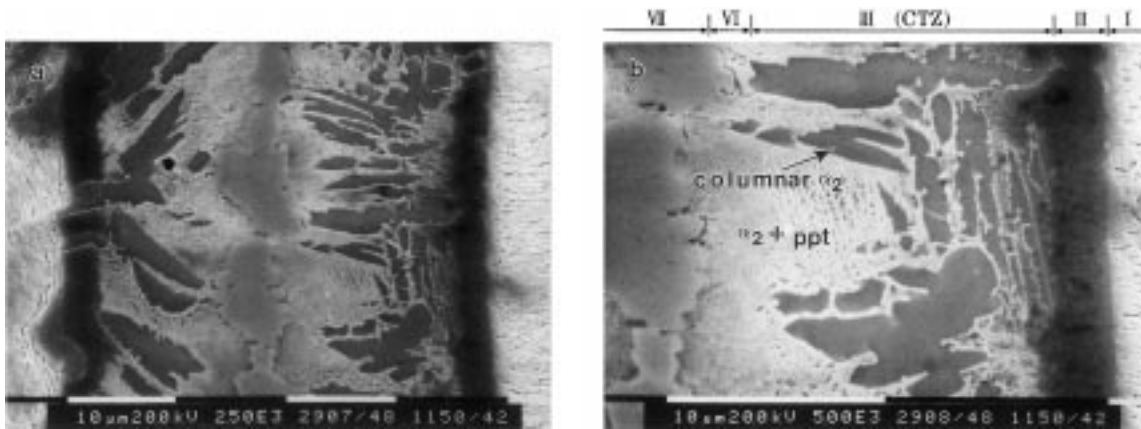

Fig. 9. The detailed SEM cross-section microstructures showing: (a) the entire joint interface; and (b) the right half-side of the 1150°C×42 s joint interface. The definition of zones I∼VII is discussed in the text.
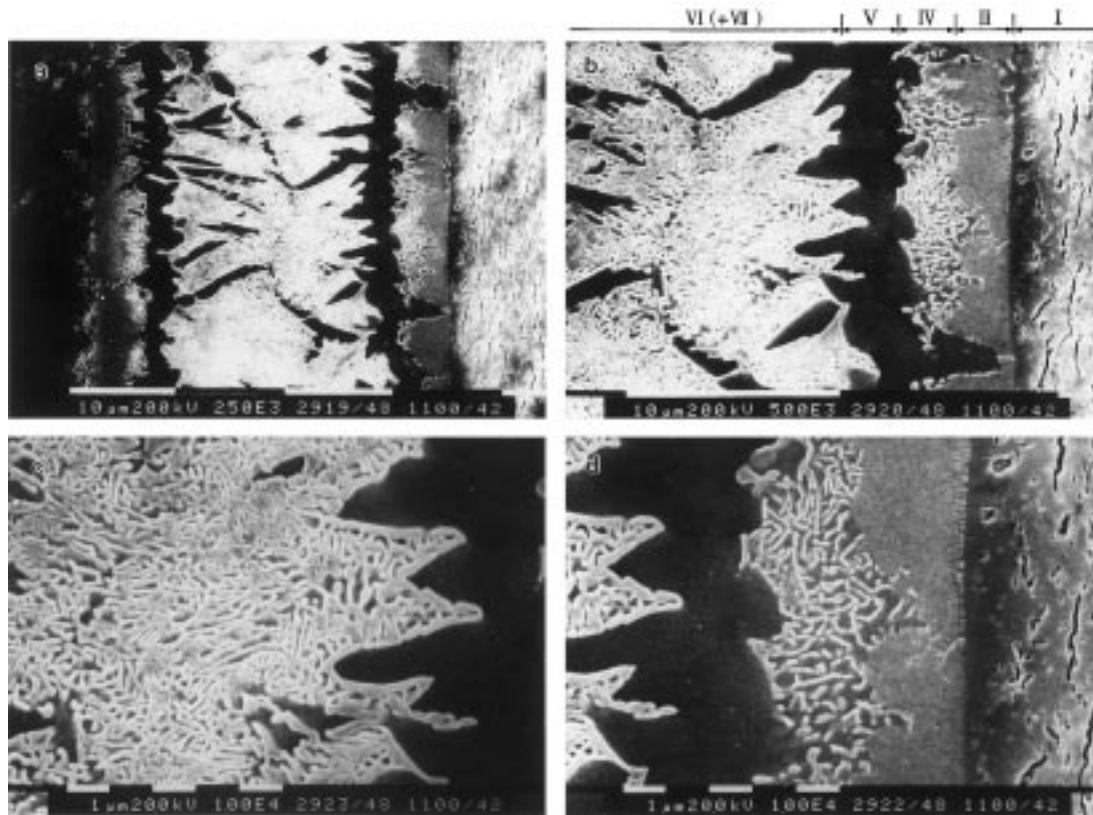

Fig. 10. The detailed SEM cross-section microstructures showing: (a) the entire joint interface; (b) the right half-side; (c) the netted precipitation zone (VI); and (d) the continuous α_2 layer (V) and the discontinuous precipitation zone (IV) of the 1100°C×42 s joint interface.

At T_w, Zone IV is also a single α-phase which is the same as the Zone II. However, its room-temperature microstructure exhibits distinct morphology from each other, as shown in Fig. 10(d). According to multiphase diffusion theories [20,21,23] and based on the Ti–Al binary phase diagram of Fig. 8, there are two possible ways to isothermally form the high Al% α-phase. One is transformed from the γ-TiAl phase due to the diffusion-out of Al atoms and the other is transformed from the $α_2$-phase due to the diffusion-in of Al atoms. As mentioned in Section 4.2.2., Zone II belongs to the former one which is merely transformed through a simple isothermal γ→α solid-state phase-transformation, while Zone IV seems to belong to the latter one which deeply involves into the complex interfacial reactions including the base-metal dissolution (stage II in Fig. 2), the isothermal solidification and the following solid-state interdiffusion (stage III in Fig. 2). Therefore, before the cooling, Zone IV should have evolved through γ + liquid filler metal → β and then β → (α + β)→$α_2$→ high Al% α phase-transformations with relatively rich Cu- and Ni- contents inside. During cooling from T_w to T_{room}, these excessively dissolved Cu and Ni atoms are expelled from the ordered $α_2$ matrix and white Cu-/Ni-rich or Cu(Ni)-base precipitates discontinuously disperse in Zone IV, as mentioned in Section 4.2.2. and shown in Fig. 10(d).

4.2.5. Zone VI: the netted precipitation zone

Zone VI corresponds to the region of the high-temperature β-Ti phase at T_w. Its room-temperature microstructure shows a unique morphology with a fully white precipitated network of Cu(Ni)-base precipitates in black $α_2$-Ti$_3$Al base. Because Zone VI has much higher Cu(Ni) content than Zone IV, the white precipitates in this zone have developed into an integral netted morphology, as shown in Figs. 9(b) and 10(c). This microstructure was resulted from the β-Ti→$α_2$ + TiCu$_2$ + Ti(Ni,Cu) ternary eutectoid reaction during cooling, identified by the XRD analyses on the fractured surfaces. (Lee and Wu, 1997, unpublished results).

4.2.6. Zone VII: the residual filler-metal zone

Zone VII is the region of residual liquid filler metal at high temperature T_w. With low Al content, this region is the only area that still keeps the liquid state before cooling, and then solidifies as an eutectic morphology during the cooling.

4.3. The effects of Nb and Cr atoms

The Section 4.2 discussion indicates that, in spite of similar microstructural morphologies between Ti–48Al–2Nb–2Cr joint interfaces and Ti$_{50}$Al$_{50}$ ones, there are still some basic differences between both joint interfaces. At the same time, the existence of Nb and

Cr atoms in Ti–48Al–2Nb–2Cr base-metal also has its own effects on the microstructural evolution of joint interfaces. Because both Nb and Cr atoms are β-stabilizers of Ti-base alloys [24], it is reasonable to suggest that their existence will enlarge the β-phase domain (shown by shadow arrows in Fig. 8) and affect the formation of continuous $α_2$ layer. Thus, the congruent temperature of $α_2$-phase in the Ti–Al binary phase diagram will be lowered and the driving force for $α_2$-phase nucleation and growth will be delayed to some extent.

Further from compared joint interfaces of Ti$_{50}$ Al$_{50}$ and Ti–48Al–2Nb–2Cr alloys, it can be found that the observed microstructure of 1100°C×42 s joint interface [Fig. 4(d) and 10] in this study is very similar to that of 1150°C×60 s joint one in Ti$_{50}$Al$_{50}$ alloy. [13,14] In addition, at T_w = 1150°C, as t_w increases, the CTZ (Zone III) in this study seems to have not disappeared or changed into Zones V and IV. These features indicate that the nucleation and growth of $α_2$ phase in Ti–48Al–2Nb–2Cr joint interfaces have indeed been delayed and the congruent temperature of $α_2$-phase in this study seems to be lowered by about 50°C, due to the existence of Nb and Cr atoms. As shown in the Ti–Al phase diagram of Fig. 8, if the β-phase region has enlarged and moved toward right- and bottom-side due to the effects of Nb and Cr atoms, the corresponding $α_2$-phase region will be forced to be smaller than the original one. Therefore, the congruent temperature of $α_2$-phase will be lowered and the degree of $α_2$-phase supercooling (ΔT) for a specific joining temperature T_w will be decreased. Since ΔT is related to the driving force for the α-Ti→ $α_2$ isothermal phase transformation [14], this smaller ΔT will make the $α_2$-layer (Zone V) more difficult to be formed in the joint interface.

Furthermore, because of the limited Cu and Ni solubility in the Ti$_3$Al($α_2$) ordered structure, once the continuous $α_2$-phase layer is formed in the joint interface, the further atomic interdiffusion between base-metal and filler-metal would be obstructed. The delayed growth of $α_2$-phase layer can prolong the growth of the columnar two-phase zone (CTZ) in the joint interface. Therefore, the observed microstructures of Ti–48Al–2Nb–2Cr joint interfaces of Fig. 4 show a wider CTZ than those of Ti$_{50}$Al$_{50}$ ones, as compared with the same joining conditions in both studies.

5. Conclusions

Infrared joining of Ti–48Al–2Nb–2Cr using Ti–15Cu–15Ni (wt%) foil as brazing filler metal was investigated at the temperature range of 1100~1200°C for 30~60 s in a flowing argon environment. The compressive tests show three types of fracture morphologies in which type I fails at the joint interface, but types II and III are fractured in the base-metal with the direction

parallel to and perpendicular to the loading axis, respectively. The cracks of type II fracture are initiated on the margin of over-flowed residual filler metal and type III fracture is cracked initially at the place of maximum bending moment. Most joined specimens were fractured through the base-metal, indicating that the infrared joined interface has relatively good joint strength. The compressive joint strength of type I specimens is about 319–322 MPa. Experimental results show that the shorter the real holding time or the higher the joining temperature, the larger the strength variation will be.

The observed interfacial microstructures of Ti–48Al–2Nb–2Cr joint interfaces indicate that seven characteristic zones can be distinguished in the joint interfaces and each characteristic zone corresponds to one or more stable phases at the T_w temperature. The observed microstructures and their evolutions of each zone are explained in detail in this study. The major difference between joint interfaces of Ti–48Al–2Nb–2Cr and $Ti_{50}Al_{50}$ alloys takes place on the base-metal interface zone and the columnar two-phase zone. The existence of Nb and Cr atoms in Ti–48Al–2Nb–2Cr alloy also has some influence on the microstructural evolution of the columnar two-phase zone and the continuous α_2-layer. Their existence seems to have lowered the congruent temperature of α_2-phase, delayed the α_2-phase integration, and enlarged the width of the columnar two-phase zone, as compared with the $Ti_{50}Al_{50}$ joint interfaces.

Acknowledgements

References

[1] Kim Y-W. JOM 1989;41:24.
[2] Kim Y-W, Dimiduk, DM. JOM 1991;43:40.
[3] Yamaguchi M, Inui H. In: Darolia R, Lewandowski JJ, Liu CT, Martin PL, Martin DB, Nathal MV, editors. Proc. Structural Intermetallics, TMS, Warrendale, PA, 1993, p. 127–142.
[4] Kim Y.-W., JOM, 1994;46:30.
[5] Patterson RA, Martin PL, Damkroger BK, Christodoulou L. Welding Journal 1990;69:39s.
[6] Baeslack III WA, Mascorella TJ, Kelly TJ, Welding Journal 1989;68:483s.
[7] Mallory LC, Baeslack III WA, Phillips DJ. Mater Sci Lett 1994;13:1061.
[8] Nakao Y, Shinozaki K, Hamada M. ISIJ International 1991;31:1260.
[9] Yan P, Wallach ER. Intermetallics 1993;1:83.
[10] Cam G, Bohm K-H, Mullauer J, Kocak M. JOM 1996;48:68.
[11] Annaji S, Lin RY, Wu SK. In: Lin RY, Chang YA, Reddy RG, Liu CT, editors. Proc. Design Fundamentals High Temperature Composites, Intermetallics, and Metal–Ceramics systems, TMS, Warrendale, PA, 1995:125–138.
[12] Blue CA, Blue RA, Lin RY. Scripta Metall Mater 1995;32:127.
[13] Lee SJ, Wu SK, Lin RY. Acta Materialia 1998;46:1283.
[14] Lee SJ, Wu SK, Lin RY. Acta Materialia 1998;46:1297.
[15] Hoffman KF, Bird RK, Discus DL. Welding Journal 1995;74:378s.
[16] Zhou Y, Gale WF, North TH. International Materials Reviews 1995;40:181.
[17] Jones SA, Kaufman MJ. Acta Metall Metal 1993;41:387.
[18] McCullough C, Valencia JJ, Levi CG, Mehrabian R. Acta Metall Mater 1989;37:1321.
[19] Baeslack III WA, Mcquay PA, Lee DS, Fletcher ED. Mater Char 1993;31:197.
[20] van Loo FJJ. Prog Solid St Chem 1990;20:47.
[21] Kirkaldy S. Diffusion in the Condensed State. London, Institute of Metals, 1987.
[22] Gegel HL. In: Collings EW, editor. The physical metallurgy of titanium alloys, ASM, Materials Park, OH, 1984.
[23] Reed-Hill RE. Physical metallurgy principles, 2nd. New York, Van Nostrand, 1973.
[24] Collings EW, The physical metallurgy of titanium alloys. Materials Park, OH: ASM, 1984.